

A review of numerical and experimental studies of the anti-fairing

Belligoli, Zeno; Dwight, Richard P.; Eitelberg, Georg; Srikumar, Sampath R.; Faleiros, David E.; Nesselrooij, Michiel van; Campenhout, Olaf van

DOI

[10.2514/6.2020-2703](https://doi.org/10.2514/6.2020-2703)

Publication date

2020

Document Version

Final published version

Published in

AIAA AVIATION 2020 FORUM

Citation (APA)

Belligoli, Z., Dwight, R. P., Eitelberg, G., Srikumar, S. R., Faleiros, D. E., Nesselrooij, M. V., & Campenhout, O. V. (2020). A review of numerical and experimental studies of the anti-fairing. In *AIAA AVIATION 2020 FORUM* (pp. 1-19). Article AIAA 2020-2703 (AIAA AVIATION 2020 FORUM). American Institute of Aeronautics and Astronautics Inc. (AIAA). <https://doi.org/10.2514/6.2020-2703>

Important note

To cite this publication, please use the final published version (if applicable).
Please check the document version above.

Copyright

Other than for strictly personal use, it is not permitted to download, forward or distribute the text or part of it, without the consent of the author(s) and/or copyright holder(s), unless the work is under an open content license such as Creative Commons.

Takedown policy

Please contact us and provide details if you believe this document breaches copyrights.
We will remove access to the work immediately and investigate your claim.



A Review of Numerical and Experimental Studies of the Anti-Fairing

Zeno Belligoli^{*}, Richard P. Dwight[†], Georg Eitelberg[‡],
Sampath R. Srikumar[§], David E. Faleiros[¶],
Michiel van Nesselrooij^{||} and Olaf van Campenhout^{**}
Delft University of Technology, 2629 HS, Delft, The Netherlands.

An anti-fairing is a concave deformation of the wall around a wing-body junction that can decrease the aerodynamic drag through the activation of a propulsive force generated by the interaction of the curved concave shape and the high-pressure region in proximity of the wing leading-edge. Although this mechanism is well understood, the dynamics of the interaction between the anti-fairing and the junction flow remain largely unexplored. This work brings together all the numerical and experimental studies of the anti-fairing to investigate its effect on turbulent quantities and the robustness of its design to changes to the incoming flow parameters, and to estimate the drag change with respect to a normal wing/flat-plate configuration. It is found that the interaction of the streamwise pressure gradient generated by the anti-fairing with the incoming boundary layer substantially reduces the shear responsible for viscous drag. Furthermore, no significant influence of the incoming boundary layer thickness on the anti-fairing performance is observed. However, a direct drag measurement with a force balance casts some doubts on the possibility to achieve large drag reductions.

I. Introduction

In aeronautics, junction flows form when a boundary layer developing on a solid surface (e.g. a fuselage) encounters a blunt object (e.g. a wing) in its path. Because of the streamwise adverse pressure gradient generated by the obstacle, the boundary layer separates and rolls upon itself forming a system of vortices. These vortices are then stretched around the object by a spanwise pressure gradient, and finally convected downstream with the rest of the flow, thus forming a system of horseshoe vortices [1]. In practice, one horseshoe vortex (HSV) is larger than the others and dominates the junction flow dynamics.

For turbulent flows, the horseshoe vortex system is not steady in terms of location, size, and circulation. In particular,

^{*}PhD Candidate, Department of Aerodynamics, z.belligoli@tudelft.nl.

[†]Associate Professor, Department of Aerodynamics, r.p.dwight@tudelft.nl.

[‡]Full Professor, Department of Flight Performance and Propulsion.

[§]Graduate Student, Department of Aerodynamics.

[¶]PhD Candidate, Department of Aerodynamics.

^{||}Guest Researcher, Department of Aerodynamics.

^{**}Guest Researcher, Department of Aerodynamics.

it appears to have an aperiodic bimodal velocity probability distribution [2] which increases the turbulence energy production and turbulent stresses in the junction region by an order of magnitude. Furthermore, the interaction of the wall boundary layer and the one developing on the wing causes high anisotropy levels in the corner region [3] and creates interference effects that tend to increase the drag [4]. Indeed, the drag of a typical wing-body junction is larger than the sum of the body drag and wing drag when separately measured in free flow [5].

A vast amount of scientific literature [6–13] has addressed the task of reducing the drag caused by junction flow phenomena with both passive and active techniques. The most studied and used solutions are the leading-edge fairing and the whole-body fairing. The former alters the shape of the wing nose in order to reduce the adverse pressure gradient generated by the leading edge, thus suppressing the onset of the horseshoe vortex [14–19]. The latter consists in wrapping the entire junction area with a fairing designed to suppress flow separation.

Whole-body fairings have been manually designed by groups of experts for decades (e.g. [20]), but recent progresses in aerodynamic shape optimization (ASO) have shown that improvements to their design are still possible [21, 22]. However, the majority of the ASO studies focused on re-designing the wing-root shape; only a handful of them [23–26] tried to optimize the fuselage shape. The results of the latter suggest that unusual shapes, much different from the typical aircraft fairing, are obtained when no constraints on the fuselage deformations are imposed. To the knowledge of the authors, Brezillon and Dwight’s optimization of the fuselage of a DLR-F6 model [23] is the first documented study showing such counter-intuitive drag-reducing fuselage shapes, namely a double-dented fairing. Inspired by these results, Belligoli et al. [27] tried to distil the main features of Brezillon & Dwight’s study by reproducing their optimization on a simple NACA 0015/flat-plate junction. The resulting optimized body shape presented itself as a shallow dent wrapped around the junction region as shown in Fig. 1a. This geometry was named *anti-fairing* to emphasize the fact that its shape is radically different from conventional fairings.

The drag force of an object depends on the product of the pressure on the solid surface of the object and the component of the surface normal in the principal direction of the flow, i.e. $p \cdot n_x$ [28]. As Fig. 1b illustrates, the curvature at the front of the anti-fairing activates the high-pressure force component which would otherwise be dormant had a normal flat wall been present. A similar pressure force is activated in the aft part of the anti-fairing. Because of incomplete pressure recovery over the wing, the net resultant of these two forces acts in the opposite direction to the drag force and thus contributes to decreasing it. The authors calculated a drag reduction of between 4.5% and 6.5% depending on the technique used to compute it. This correlates with the observed reduction in the momentum deficit in the wake when comparing a wing/anti-fairing configuration to a wing/flat-plate configuration (baseline) as shown in Fig. 2a and Fig. 2b. Additionally, the anti-fairing causes the boundary layer to separate closer to the wing, and a displacement of the HSV cores away from the wing symmetry plane. As Fleming et al. [29] explained in their work, these observations are linked to an increase in the Momentum Deficit Factor $MDF = Re_T Re_\theta$ and, consequently, in the momentum thickness of the boundary layer.

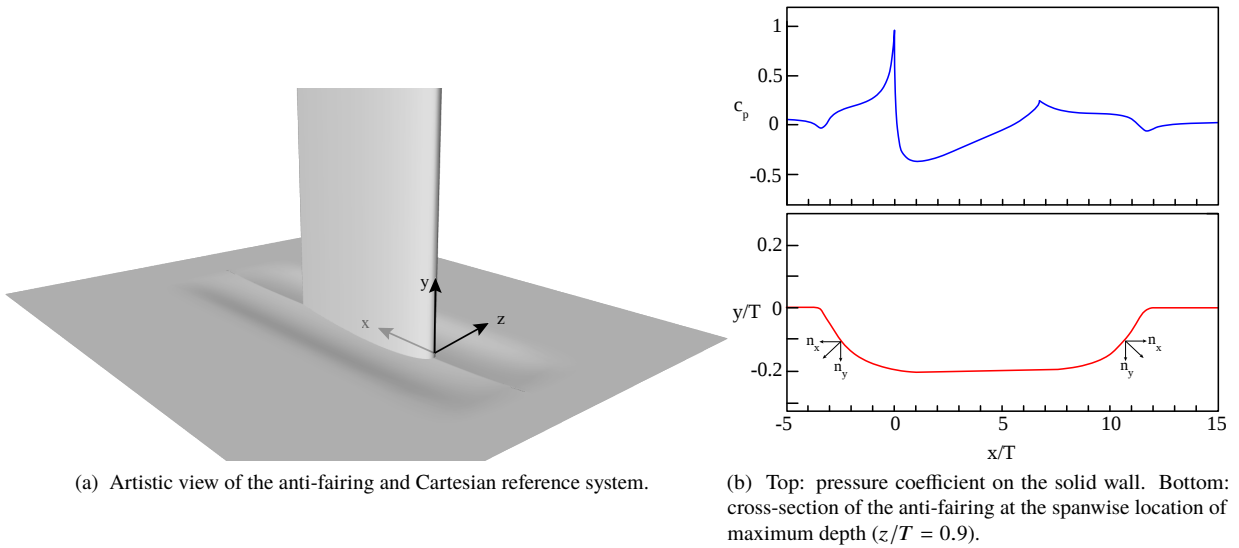


Fig. 1 Anti-fairing view and working mechanism.

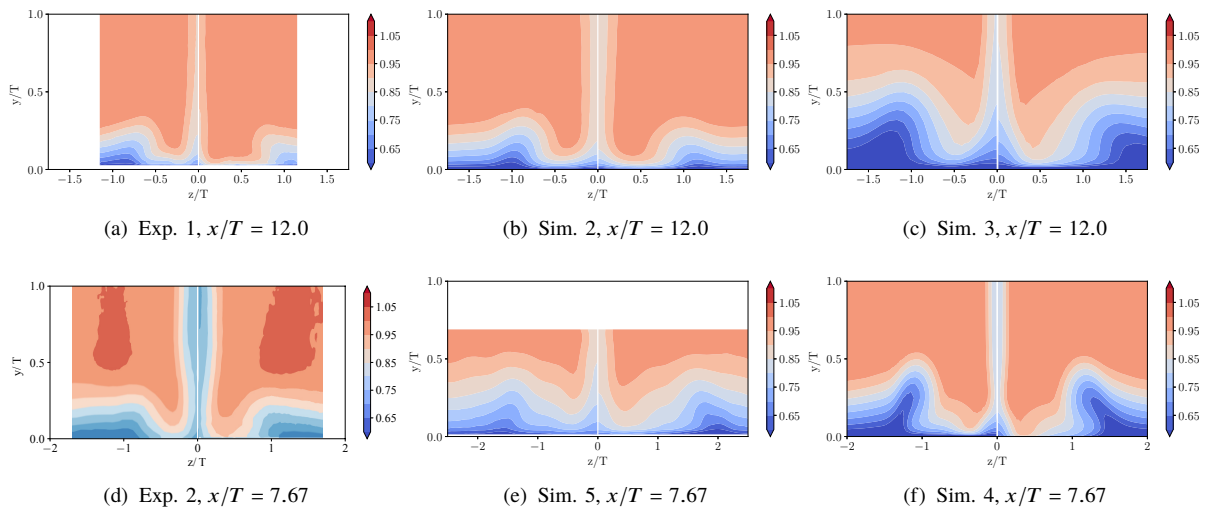


Fig. 2 Normalized streamwise velocity in the wake of the junction area for all the numerical and experimental studies on the anti-fairing. Left: Baseline; Right: Anti-fairing. Differences in the wake are due to the different flow conditions and geometries tested.

Table 1 List of numerical studies on the anti-fairing.

Case name	Solver	Wing geo.	Domain	# Mesh points	U_∞ [m/s]	c [m]	Turb. model	y^+
Sim. 1	SU2	NACA 0015	Structured	$1.6 \cdot 10^6$	20.0	0.75	SA	1
Sim. 2	STAR-CCM+	NACA 0015	Hybrid	$1.15 \cdot 10^7$	20.0	0.75	SA	1
Sim. 3	OpenFOAM	NACA 0015	Structured	$6.0 \cdot 10^6$	27.0	0.20	SST	50
Sim. 4	OpenFOAM	Rood	Structured	$6.0 \cdot 10^6$	27.0	0.305	SST	50
Sim. 5	INCA	Rood	Cartesian	$2.5 \cdot 10^7$	27.0	0.305	n.a.	50

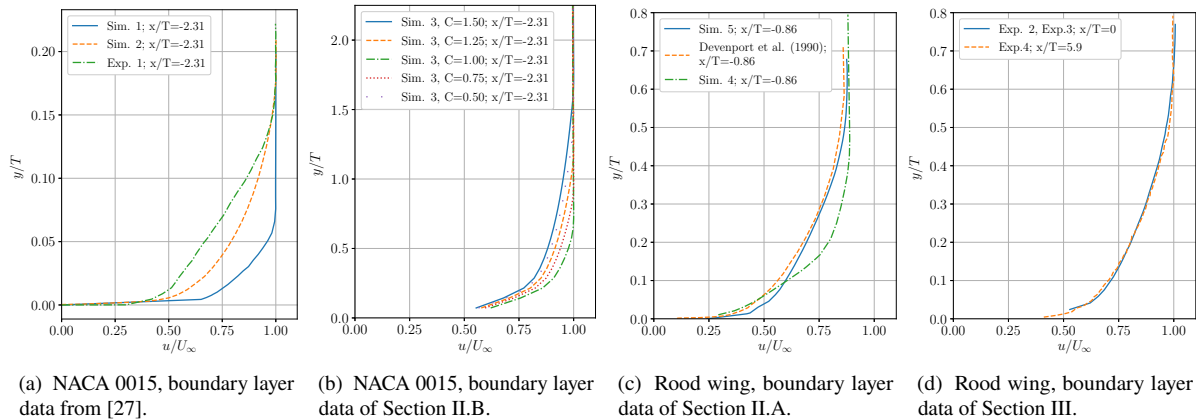
Table 2 List of experimental studies on the anti-fairing.

Case name	Type of experiment	Wing geo.	U_∞ [m/s]	c [m]
Exp. 1	Stereo PIV	NACA 0015	15.0-30.0	0.75
Exp. 2	Stereo PIV	Rood	10.0	0.20
Exp. 3	Tomo-PTV	Rood	10.0	0.20
Exp. 4	Balance	Rood	20.0-35.0	0.137

Over the last few years, the anti-fairing has been used as reference test case for a number of numerical and experimental junction-flow studies carried out at the Delft University of Technology. It must be mentioned that these studies were conducted at several different flow conditions, and with different wing shapes as shown in Tables 1 and 2, and Figures 2 and 3. Reporting the main findings of these studies is the purpose of this work. In particular, in Section II, we present the main results of all the CFD studies on the AF; similarly, Section III summarizes the findings of all the experimental studies. Final considerations and ideas for future studies are then reported in the Section IV.

II. Numerical Studies

The work of Belligoli et al. [27] presented the first two RANS studies of the anti-fairing and demonstrated the reproducibility of the results on two different CFD solvers, namely SU2 [30–32] and STAR-CCM+. In this Section,

**Fig. 3 List of all the boundary layers used for numerical or experimental studies of the anti-fairing.**

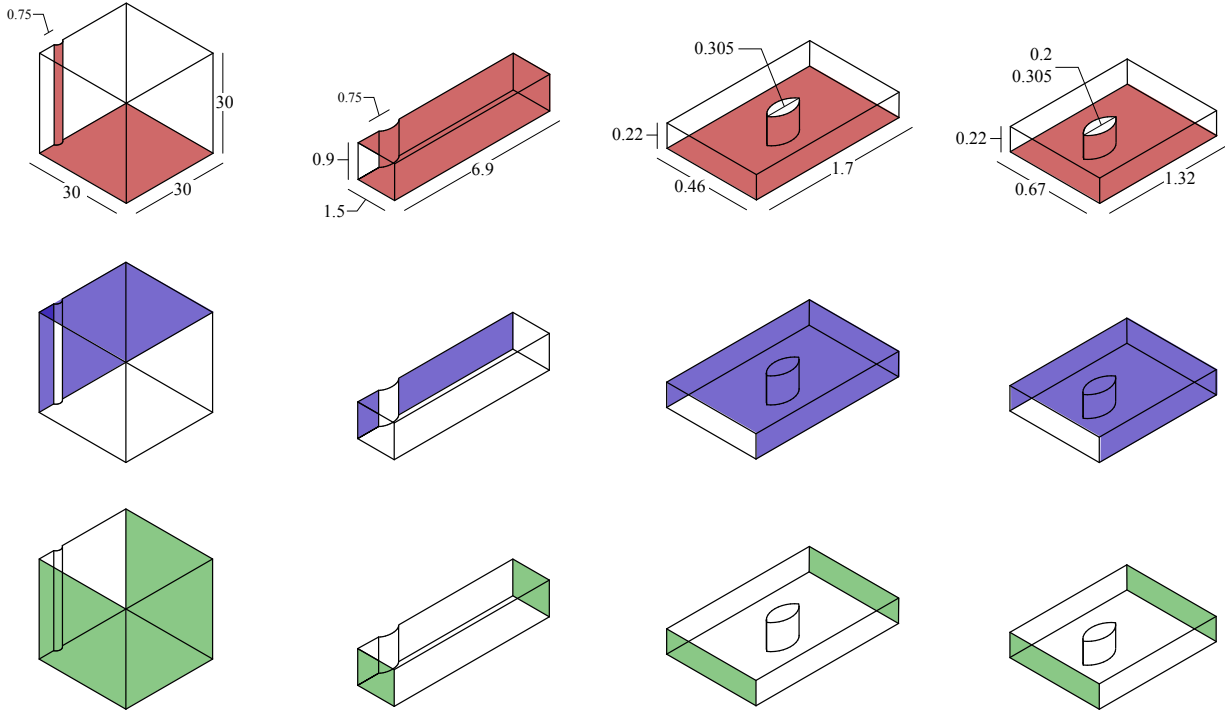


Fig. 4 Overview of the domain sizes (in meters) used for the numerical simulations. Red: no-slip boundary condition; Blue: symmetry boundary condition; Green: inlet/outlet/characteristic boundary conditions. From the left to right: SU2, STAR-CCM+, INCA, OpenFOAM.

the results of a wall-modeled Large Eddy Simulation (LES) are used to study the behaviour of vorticity and turbulent kinetic energy in the junction region. In addition, a RANS sensitivity analysis of the anti-fairing performance with respect to changes to its shape and incoming flow conditions is carried out to ascertain the robustness of the design.

A. Large Eddy Simulations

Based on their study of the capability of RANS turbulence models to reproduce junction flow phenomena, Apsley et al. [33] concluded that RANS can be used to study qualitative features of the flow, while LES are needed to obtain accurate quantitative results. Hence, in this Section we discuss a LES study of the anti-fairing, focusing on the evolution of two quantities that have been overlooked in [27]: the streamwise vorticity and the turbulent kinetic energy.

As usual, the results for the wing/anti-fairing (AF) configuration are compared with those for a baseline wing/flat-plate (BS) configuration. To align ourselves with the junction flow literature, we choose to simulate a Rood wing instead of a NACA 0015. The flow conditions, shown in Table 1, are the same as in the experiment of Devenport and Simpson [2]. For the simulations, we make use of the in-house finite volume solver INCA, which performs implicit large eddy simulations, whereby the numerical discretization and subgrid-scale model are merged through the discretization of the advective terms based on the adaptive local deconvolution method [34, 35]. A third-order Runge-Kutta scheme is used for the temporal discretization, and a second-order accurate central difference scheme for the viscous and pressure

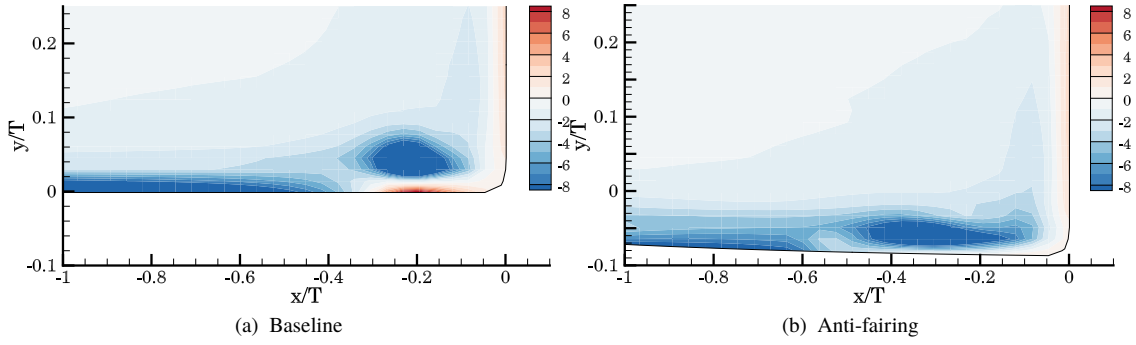


Fig. 5 Contours of normalized streamwise vorticity $\omega_z \frac{T}{U_\infty}$ in the symmetry plane ($z/T = 0$).

gradient terms. For this incompressible case, pressure-velocity coupling is obtained by means of a Bi-Conjugate Gradient Stabilized Poisson solver.

A conservative immersed interface method [36] is applied to map the junction geometry onto the staggered, Cartesian grid. Adaptive mesh refinement is used to refine the grid in the regions close to the solid walls, resulting in a total of 25 million cells with a $y^+ \approx 50$ based on the free-stream speed. Further refinement of the mesh was constrained by the available computational resources. Hence, a wall model based on the generalized wall functions (GWF) [37] is applied to model the flow between the log-layer and the adiabatic wall. The validation of the LES against experimental data, omitted here for brevity but available in [38], shows good agreement for the boundary layer development, wall-pressure contours, shape and magnitude of the vorticity field. Good qualitative agreement for the turbulent kinetic energy is also obtained, but its magnitude is half of that of the experimental data of [2] and the LES data of [39] due to insufficient mesh resolution near the wall. Nevertheless, one can still obtain meaningful information from the comparison of the relative turbulent kinetic energy magnitude between the anti-fairing and the baseline.

Figure 5 shows the vorticity, normalized by the ratio of wing thickness T to free-stream speed U_∞ , in the symmetry plane at the wing leading-edge. In the AF case, the HSV is stretched along the streamwise direction in a region close to the wall. The ejection of positive vorticity from the wall separating the boundary layer from the HSV is observed more upstream ($x/T = -0.55$) than in the baseline case ($x/T = 0.35$), and similar considerations hold for the HSV core. As already noted at the beginning of Section I, these observations are linked to an increase in momentum deficit factor (MDF) with respect to the baseline case. From the symmetry plane, the vortex stretches around the wing and is convected downstream by the mean flow. At the same time, its strength is slowly dissipated by the action of viscosity. Interestingly, although the baseline HSV has higher peak vorticity at the symmetry plane than the anti-fairing HSV, its rate of dissipation as it moves around the wing is faster as shown in Fig. 7a. This suggests that the magnitude of turbulent dissipation is reduced by the action of the anti-fairing.

Figure 6 shows the normalized turbulent kinetic energy in the symmetry plane. Although the results are affected by the limited grid resolution, it is evident that the anti-fairing has substantially lower turbulent kinetic energy than the

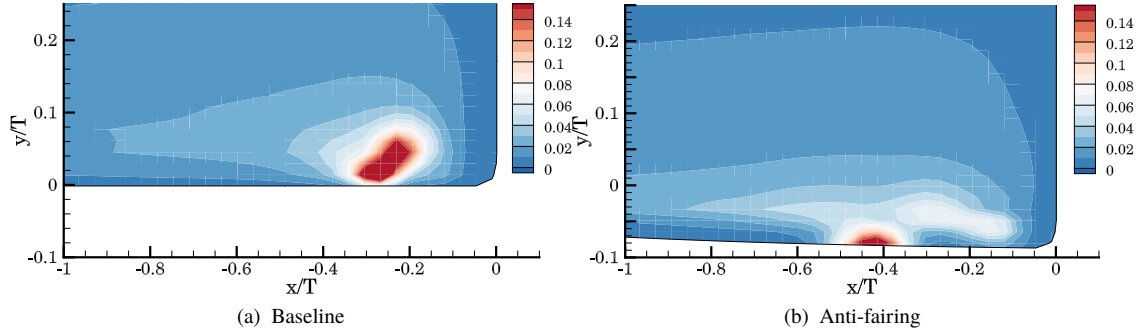


Fig. 6 Contours of normalized turbulent kinetic energy $\frac{k}{U_\infty^2}$ in the symmetry plane ($z/T = 0$).

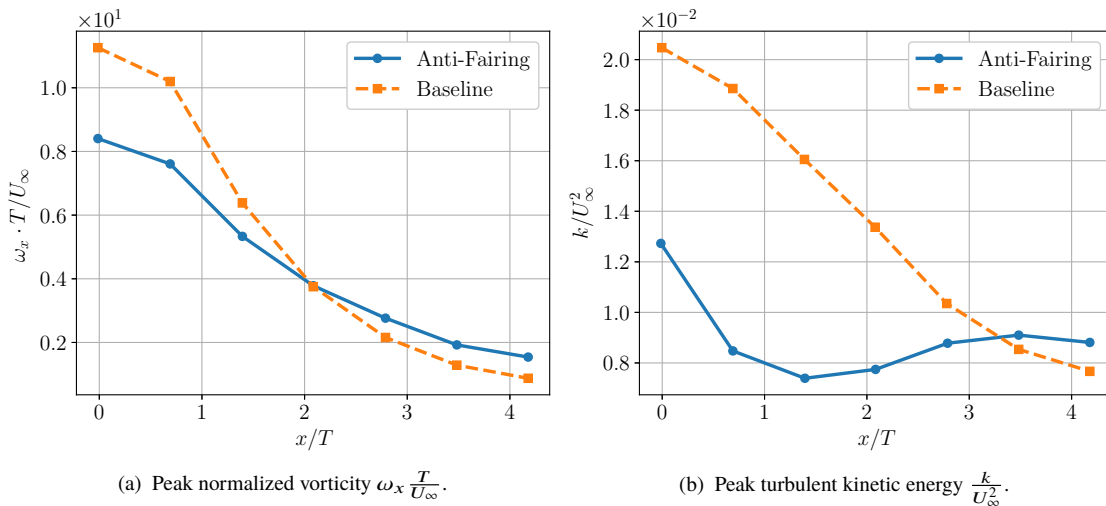


Fig. 7 Vorticity and turbulent kinetic energy in the vortex core at different streamwise locations.

baseline. This situation holds for most of the course of the HSV around the wing as shown in Fig. 7b. The presence of this phenomenon is also confirmed by the experimental results of Section III.A, thus supporting the claim that peak turbulent kinetic energy is reduced in the first half of the anti-fairing.

In the streamwise direction, the anti-fairing presents a convex-concave curvature at the front and concave-convex curvature at the back as shown in Fig. 1b. These two curved parts are connected by a zone of essentially zero curvature where the wing is located. As Fig. 8a shows, the turbulent boundary layer approaching the start of the anti-fairing first encounters a favourable streamwise pressure gradient, followed by an adverse pressure gradient due to the concave curve. At approximately $x/T = -1$, the influence of the wing sharply generates a region of favourable pressure gradient, followed by a region of mild adverse pressure gradient until $x/T = 6$. Finally, the concave-convex curvature at the back of the anti-fairing generates a favourable and adverse pressure gradient, respectively.

It is interesting to observe the inverse correlation of the streamwise pressure gradient with the shear component $\partial u / \partial y$. An adverse pressure gradient reduces the wall-normal shear, and vice-versa. The favorable pressure gradient

generated by the initial part of the wing makes $\partial u/\partial y$ increase rapidly both in the baseline and anti-fairing case. However, the short region of adverse streamwise pressure gradient in the anti-fairing ahead of the wing causes a drop in wall-normal shear. This influences its overall magnitude which remains substantially lower than that of the baseline. Similar effects to those of Fig. 8 are observable at other lateral locations z/T along the anti-fairing width. Sufficiently far from the junction region, $\partial U/\partial y$ is orders of magnitude larger than the other components of the velocity gradient contributing to the viscous drag. This implies that the anti-fairing not only reduces drag by creating a propulsive pressure force, but also by decreasing the magnitude of viscous stresses. Belligoli et al. [27] already hinted at this possibility, but the present analysis, together with the results of Section II.B offer an additional evidence.

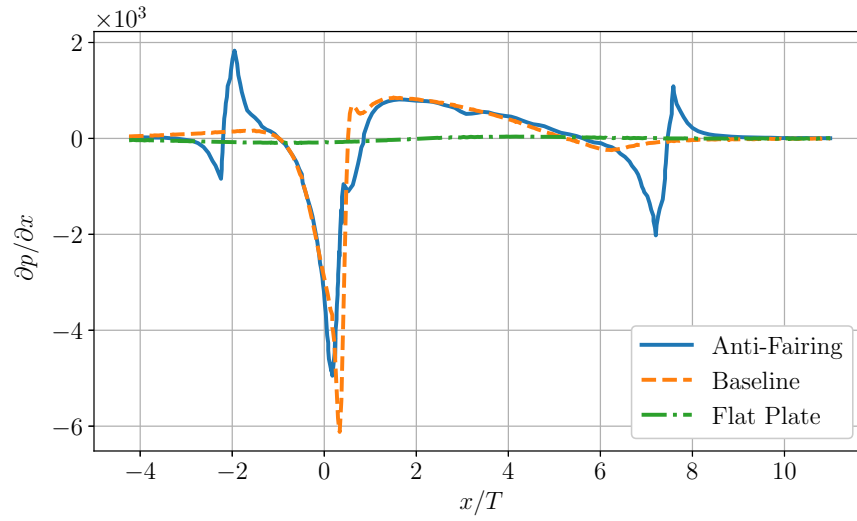
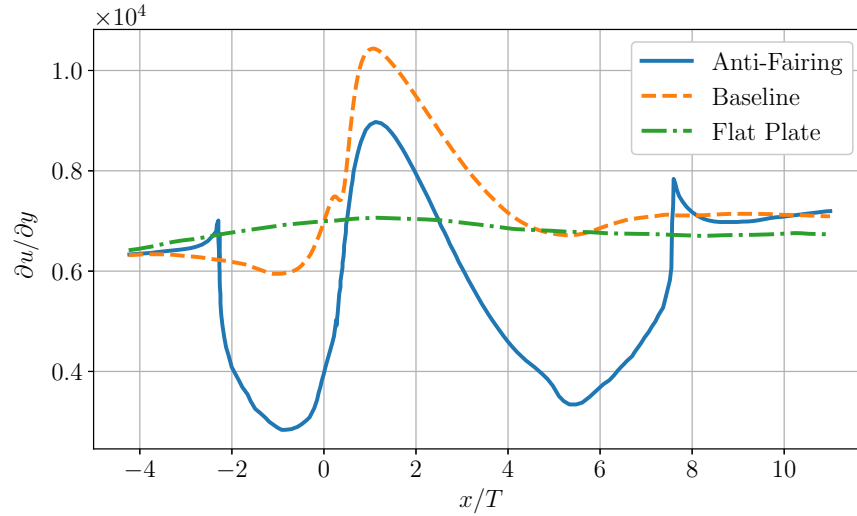
It is somewhat surprising how such a small region of adverse pressure gradient ahead of the wing has such a large impact on the wall-normal shear. It is also possible that more complex curvature effects are present as the two-dimensional incoming turbulent boundary layer encounters the convex-concave shape at the anti-fairing start. Indeed, many of the phenomena observed in this Section are also typical of curvature effects on boundary layers [40–44]. This is one potential topic for future studies.

B. Sensitivity Analysis

The incoming boundary layer shape and characteristics are one of the most important factors influencing the features of the horseshoe vortex such as vortex size and the magnitude of the turbulent quantities [29]. Therefore, this Section studies the performance of different anti-fairing depths and boundary layer thicknesses in relation to drag reduction. For the subsequent set of simulations, we make use of the open-source CFD solver OpenFOAM.

A NACA 0015 wing with a chord $c = 0.2\text{m}$ is used for this sensitivity study, for which a matrix of 30 test cases is constructed based on five different boundary layers and six different anti-fairing depths. The reference boundary layer shape at $x/T = -2.15$ is the same as in the study of Devenport and Simpson [2], while the reference anti-fairing depth is the one obtained from the ASO in [27]. From here, the other four boundary layers are obtained by scaling the reference one with the factors $C = 0.5, 0.75, 1.25, 1.5$ as shown in Tab. 3 and Fig. 3b. Similarly, five additional anti-fairings were generated by scaling the initial AF geometry in the wing's spanwise direction such that the maximum thickness was $K \cdot d_{\max}$, with d_{\max} being the maximum depth of the original anti-fairing, and $K = 0.0, 0.5, 0.75, 1.25, 1.5$. Note that $K = 0$ corresponds to having an anti-fairing with zero depth, i.e. a normal flat plate. The details for these cases are given in Table 4.

The computational domain for this sensitivity study is shown in Fig. 4. The origin of the coordinate system is aligned with the flat part of the plate and located at the leading edge of the wing. The inlet and outlet planes are located at $x/T = -10.2$ and $x/T = 25.3$, respectively; the side boundaries are placed at $z/T = \pm 14.67$, and the top plane at $y/T = 7.3$. A velocity profile of thickness δ_{IN}^{99} is specified at the inlet, while a constant total pressure is prescribed at the outlet. A symmetry boundary condition is used for the side and top boundaries and a no-slip condition is used on the

(a) Pressure gradient: $\frac{\partial p}{\partial x}$ (b) Wall shear stress: $\frac{\partial u}{\partial y}$ **Fig. 8** Pressure gradient and shear stress on the wall at the spanwise location of maximum depth ($z/T = 0.9$).**Table 3** List of inlet boundary layer thicknesses considered.

Case Number (<i>i</i>)	Case name	δ_{IN}^{99}/T
1	BL _{0.5}	0.552
2	BL _{0.75}	0.828
3	BL _{1.0}	1.103
4	BL _{1.25}	1.379
5	BL _{1.5}	1.665

Table 4 List of different anti-fairing depths considered.

Case number (<i>j</i>)	Case name	d_{max}/T
1	AF _{0.0}	0.0
2	AF _{0.5}	0.104
3	AF _{0.75}	0.156
4	AF _{1.0}	0.208
5	AF _{1.25}	0.260
6	AF _{1.5}	0.312

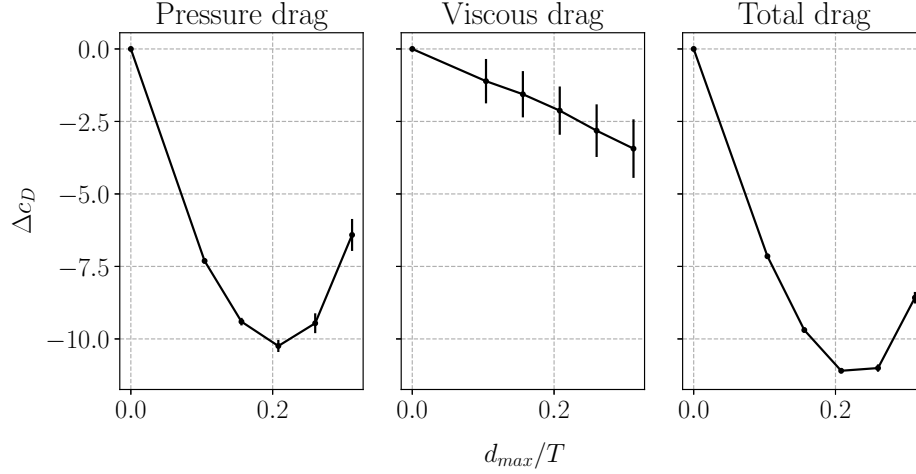


Fig. 9 Effect of anti-fairing depth and incoming boundary layer thickness on the drag reduction. The line represent the mean drag reduction for different incoming boundary layer thicknesses. The error bars correspond to one standard deviation from the mean. The source of the variability for viscous drag data is unknown.

solid boundaries.

A structured mesh with approximately 6 million points and a $y^+ = 50$ is used. The steady, incompressible RANS equations are solved using OpenFOAM's *simpleFoam* solver. Second-order upwind discretization schemes are used for the convective and diffusive terms. The linear systems arising from the discretization of the governing equations are solved using the generalized geometric-algebraic multi-grid (GAMG) solver. The closure of the RANS equations is provided by Menter's $k - \omega$ SST model [45] in conjunction with wall functions. The drag coefficient is obtained by normalizing the drag force with the free-stream dynamic pressure and the reference area $A_{ref} = T \cdot b$, where T is the maximum thickness of the wing, and b is the wing-span of the configuration with $K = 1.0$. The drag deltas (in drag counts) are computed as

$$\Delta c_D = (c_{D,ij} - c_{D,31}) \cdot 10^4, \quad (1)$$

where $c_{D,ij}$ is the drag coefficient of the configuration with the i -th boundary layer thickness and the j -th anti-fairing depth. The drag coefficient $c_{D,31}$ corresponds to the baseline case, i.e. a simple wing/flat plate junction.

In order to isolate each contribution to the total drag, Fig. 9 reports the pressure and viscous drag separately. The Δc_D values are an average of the results for the different boundary layer thicknesses tested. The error bars correspond to one standard deviation from the mean. The first column shows the variation in pressure drag coefficient as a function of anti-fairing depth. We observe higher drag reductions with deeper anti-fairings because of the enhanced pressure propulsive effect due to the increase in static pressure upstream of the wing: the cross-sectional area of a streamtube increases when this encounters the front part of the anti-fairing, thus slowing the flow down; this, in turns, increases the static pressure in front of the wing which enhances the propulsive effect explained in Section I.

As the anti-fairing gets deeper, also the viscous drag component decreases due to the adverse pressure gradient at the beginning of the anti-fairing causing a smaller wall-normal shear at the wall. The fact that the anti-fairing has a consistently smaller viscous drag than the baseline (see Fig. 9) confirms the conclusions of the analysis of Section II.A.

The sum of pressure and viscous drag returns the total drag of the configuration. It is clear that the main contribution to the drag reduction comes from the propulsive pressure mechanism described in Section I, and thus that the viscous drag reduction is only a secondary mechanism. It is also evident that the maximum drag reduction is obtained close to the anti-fairing depth produced by the original optimization, thus adding confidence to the results of Belligoli et al. [27].

Given the small standard deviation of the results for the total drag, we can conclude that the effect of boundary layer thickness on the drag reduction caused by the anti-fairing is negligible.

III. Experimental Studies

The only previously available experimental data on the anti-fairing come from the stereo-PIV in the wake of the junction done in [27]. The authors observed a significant reduction in momentum deficit (see Fig. 2a) which is a good indication of drag reduction. This Section presents the main findings of two new experimental studies of the anti-fairing. In Section III.A, tomographic PTV is used to obtain volumetric data in the junction region. Section III.B reports the results of a direct drag measurement of the anti-fairing using a novel force balance developed by Dimple Technologies [46].

A. Tomographic PTV

The numerical results of Section II are sufficient to build a picture of the main effects of the anti-fairing on the flow. However, the uncertainties associated to RANS turbulence modeling and LES grid resolution call for further experimental validation of the numerical results. For this reason, we devised a wind-tunnel experiment using both stereo-PIV and tomographic-PTV. With the former technique we obtain results similar to those of the experiment in Belligoli et al. [27], while with the latter we can visualize the 3D velocity and Reynolds-stress fields in the junction region.

Two configurations, consisting of a Rood wing perpendicularly attached either on a flat-plate or the anti-fairing, are tested. The wing chord is $c = 0.2\text{m}$ and the model spans the entire wind-tunnel height, such that its span is $b = 0.4\text{m}$. Zig-zag tape is placed at the maximum thickness of the wing model and at an appropriate distance upstream of the wing-leading edge to force transition. The resulting turbulent boundary layer at the wing leading-edge can be seen in Fig. 3d. All experiments are conducted at a wing speed of 10m/s . As shown in Fig. 10, a transparent test section allows an easy optical access for the two and three high-speed cameras used for stereo-PIV and tomo-PTV, respectively. For tomo-PTV, a relatively large measurement domain of about $1,400\text{cm}^3$ has been achieved thanks to the use of helium-filled soap bubbles as seeding medium [47, 48]. More details on both experimental setups can be found in [49].

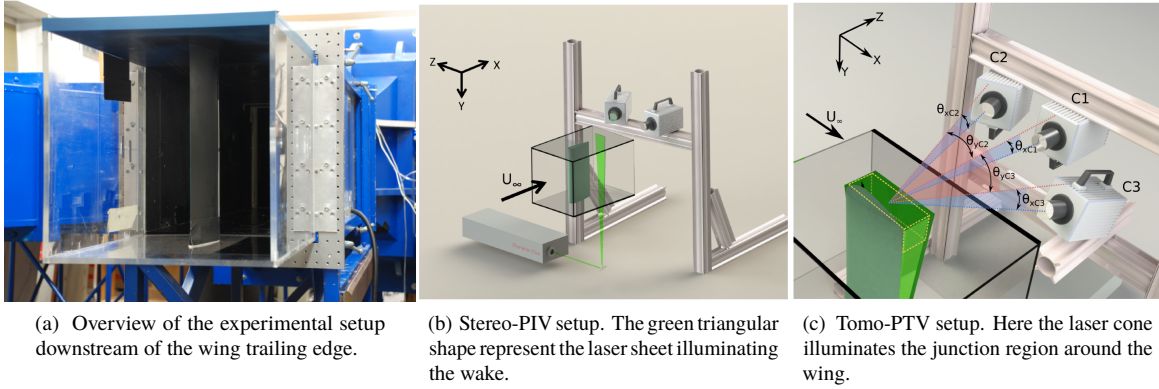


Fig. 10 Details of the experimental setups.

The streamwise velocity distribution in the wake at $x/T = 7.67$ for the baseline and anti-fairing configuration is shown in Figure 2d. Because of the different experimental conditions, only qualitative results with the stereo-PIV results of Belligoli et al. [27] can be made. Nonetheless, a comparable velocity deficit reduction is observed also in our results. Quantitatively, this corresponds to 8% less momentum deficit than the baseline case, thus constituting additional evidence in favour of the drag-reducing action of the anti-fairing.

Figures 11 and 12 show the contours of the diagonal component of the normalized Reynolds stress tensor. At $x/T = 1.5$, the anti-fairing has lower R_{xx} and R_{zz} than the baseline configuration, and a comparable R_{yy} . This evidence is in line with the observations of Section II.A about the lower turbulent kinetic energy $k = (\overline{u'u'} + \overline{v'v'} + \overline{w'w'})/2$ of the anti-fairing with respect to a normal wing/flat-plate configuration. Figure 12 shows that this effect, although damped, continues at least up to $x/T = 4.0$, which is close to the wing trailing-edge and before the concave/convex part of the back of the anti-fairing.

B. Balance measurements

The accurate experimental measurement of the drag of a wing-body junction is a complicated endeavour. One can measure the velocity deficit sufficiently downstream of the test object and compute the drag as a momentum deficit. This technique relies on several assumptions that are not always applicable due to spatial limitations of the experimental setup. A second way is to make use of a force balance. However, the drag is usually one order of magnitude smaller than the lift and, as such, its measurement is more affected by uncertainties due to repeatability and system accuracy.

For a direct measurement of the anti-fairing drag, we did a wind-tunnel test using a newly developed force balance system with a flat-plate repeatability of 0.1% at 35m/s. The experiment was carried out in the M-Tunnel of the Delft University of Technology, an open-jet low-speed tunnel with a $0.4 \times 0.4\text{m}^2$ cross-section, and a turbulence intensity below 0.8%. A Rood wing with a chord $c = 0.137\text{m}$ and span $b = 0.110\text{m}$ was used, and a wing/flat-plate and a wing/anti-fairing configurations were 3D-printed and tested. The boundary layer was fully turbulent for all measured flow

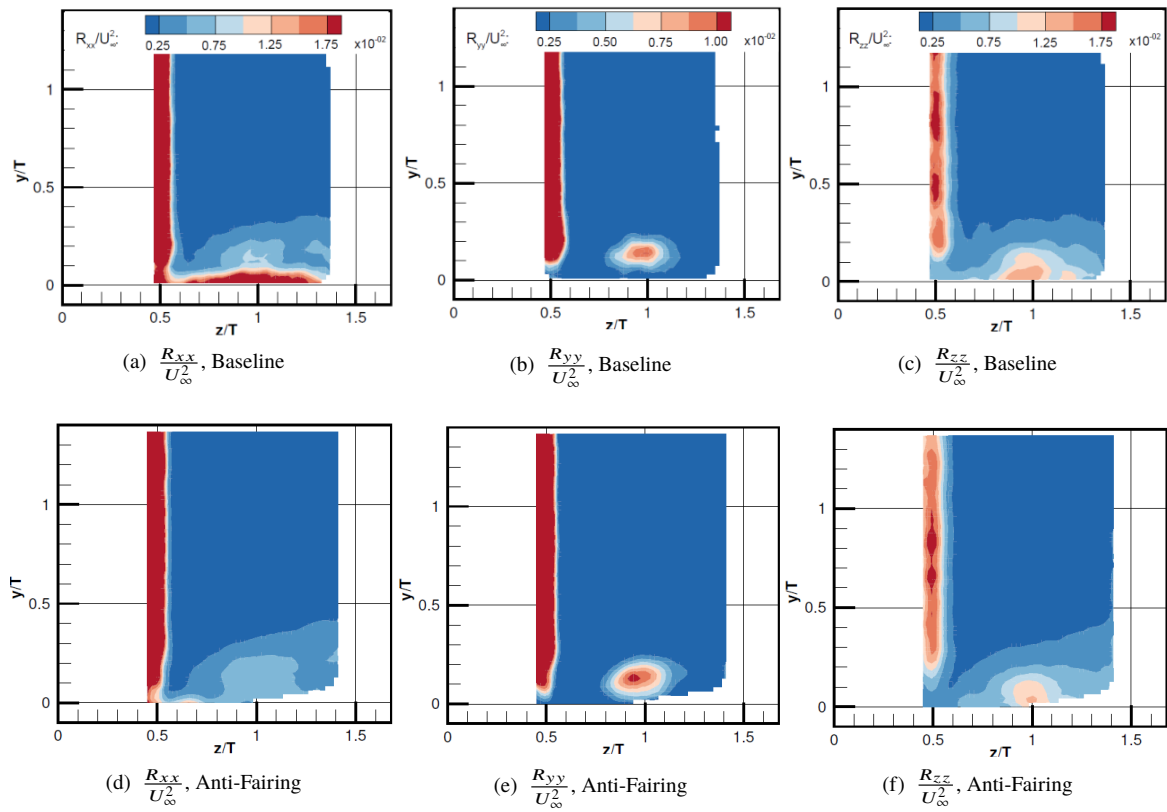


Fig. 11 Contours of the diagonal components of the normalized Reynolds-stress tensor at $x/T = 1.5$.

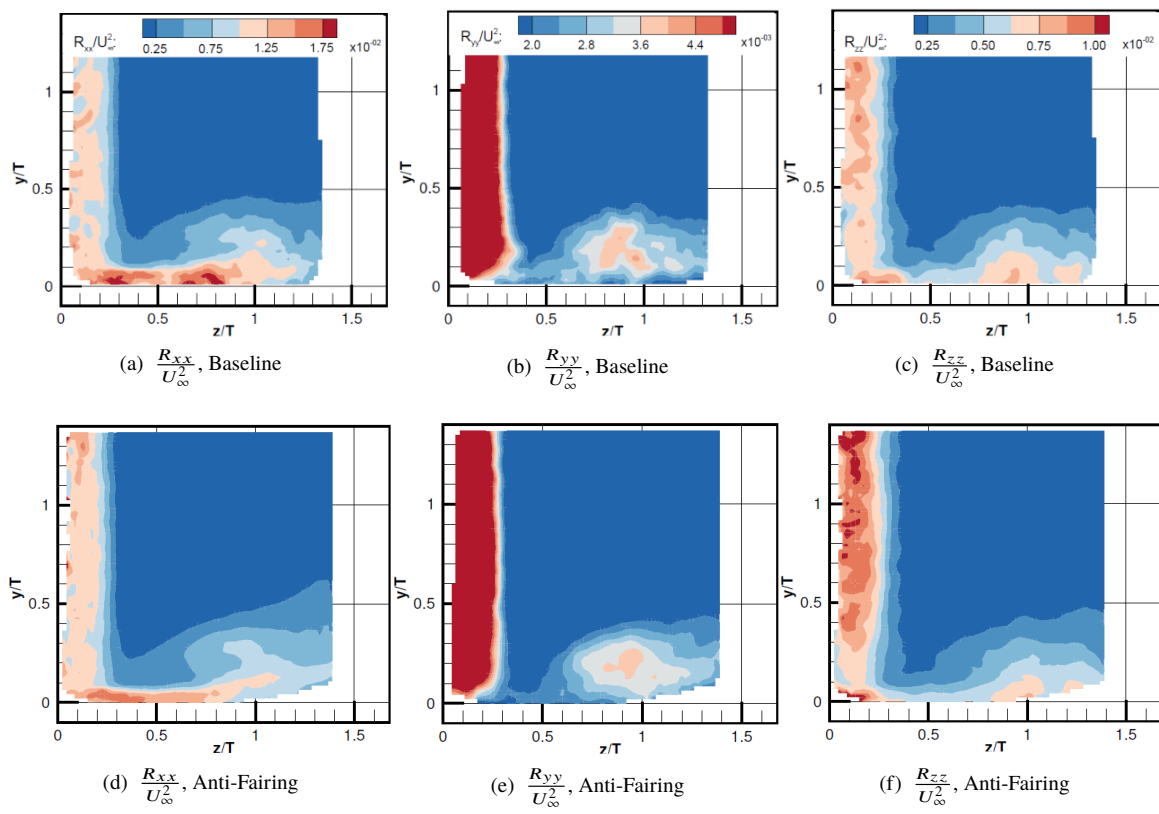
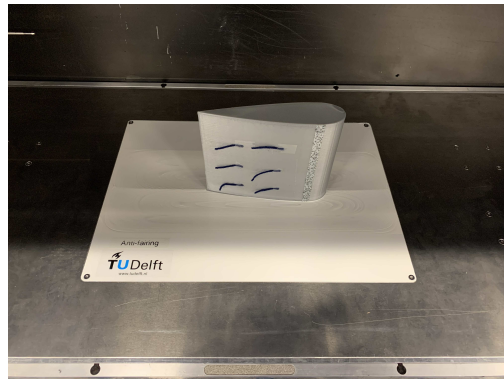
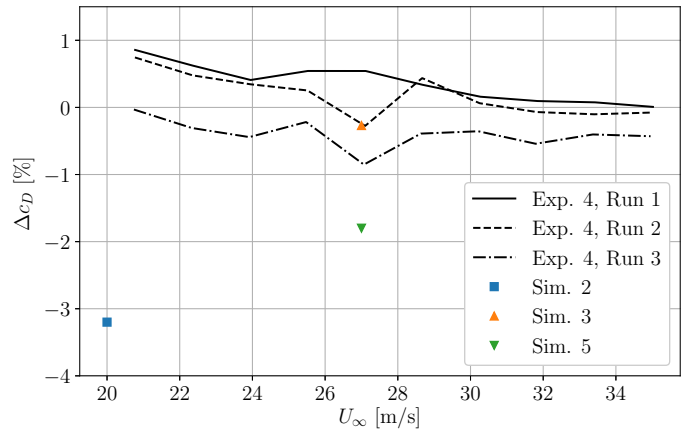


Fig. 12 Contours of the diagonal components of the normalized Reynolds-stress tensor at $x/T = 4.0$.



(a) Overview of the wing/body model.



(b) Mean drag difference between a wing/flat-plate and wing/anti-fairing configurations as a function of free-stream speed.

Fig. 13 Details of the experimental setup and results of the balance measurement.

velocities, while the boundary layer forming over the wing was forced to transition by means of a strip of carborundum roughness at the location of maximum thickness as shown in Fig. 13a. The turbulent boundary layer of Fig. 3d was measured in an undisturbed flow region at $x/T = 5.4$ downstream of the wing trailing-edge. A range of free-stream velocities were tested, from 20.0m/s to 35.0m/s. The drag coefficient is obtained by dividing the drag force measured by the balance by the product of the dynamic pressure and a reference area $A_{\text{ref}} = T \cdot b$. It should be noted that the wing aspect ratio is lower than unity and that its span is only a quarter of the wind-tunnel height. These characteristics make this experiment different from the other experimental and numerical studies on the anti-fairing, since the vortex shed by the wing-tip can influence the junction flow dynamics.

Fig 13b shows the drag difference between the baseline and anti-fairing configurations of three different experimental runs alongside some data from the simulations. A Reynolds-number effect is observed since Δc_D is positive at low speeds and asymptotically declines towards a stable value at the highest speeds. The maximum measured drag increase is about 1 percent at the lowest speed. On the other hand, the maximum measured drag decrease is about 0.4% at the highest speeds. However, the relative change in drag at that point is less than 0.2% and falls within the margin of error of the measurement. Furthermore, we observe that the Δc_D computed numerically seems to be too optimistic in terms of achievable drag reduction.

IV. Conclusion

This work reviewed all the numerical and experimental studies of the anti-fairing, a concave deformation of the wall around wing/body junctions that reduces the aerodynamic drag. The main drag-reducing mechanism is the activation of a propulsive pressure force thanks to the interaction of the curved front part of the anti-fairing and the high wall pressure

on the wall resulting from the presence of the wing.

This work showed that a secondary drag-reducing mechanism exists. This is due to the combined action of the streamwise pressure gradient, caused by the anti-fairing and the wing, which reduces the wall-normal shear of the streamwise velocity and, consequently, viscous drag.

A second finding is that the incoming boundary layer thickness has no significant influence on the anti-fairing performance. The anti-fairing depth affects the magnitude of the drag reduction, with the optimum depth being close to the one obtained by the original optimization of Belligoli et al. [27].

A balance measurement of the drag force does not show a statistically significant drag effect, possibly due to the effect of the wake of the wing tip and small wing aspect ratios.

Future numerical studies should focus on a wall-resolved Large Eddy Simulation of the anti-fairing. This would allow to obtain an accurate estimate of the drag reduction, and an analysis of the alteration caused by the anti-fairing to the standard junction flow dynamics. More attention should be paid to the effects of wall curvature on the boundary layer and in relation to drag reduction. Furthermore, the sensitivity to changes in Reynolds and Mach number, as well as angle of attack should be assessed.

Acknowledgements

The authors would like to thank Ka Hin Yeung for helping with the experiments with tomographic PTV, and Prof. Stefan Hickel for the help in preparing the LES simulations with INCA.

References

- [1] Simpson, R., "Junction flows," *Annual Review of Fluid Mechanics*, Vol. 33, No. 1, 2001, pp. 415–443. doi:10.1146/annurev.fluid.33.1.415.
- [2] Devenport, W., Agarwal, N., Dewitz, M., Simpson, R., and Poddar, K., "Effects of a fillet on the flow past a wing-body junction," *AIAA journal*, Vol. 28, No. 12, 1990, pp. 2017–2024. doi:10.2514/3.10517.
- [3] Gand, F., Deck, S., Brunet, V., and Sagaut, P., "Flow dynamics past a simplified wing body junction," *Physics of Fluids*, Vol. 22, No. 11, 2010, p. 115111. doi:10.1063/1.3500697.
- [4] Pierce, F., and Nath, S., "Interference drag of a turbulent junction vortex," *Journal of fluids engineering*, Vol. 112, No. 4, 1990, pp. 441–446. doi:10.1115/1.2909423.
- [5] Hoerner, S., "Fluid Dynamic Drag. 1965," *Bricktown, NJ: Published by the author*, 1965.
- [6] McGinley, C., "Note on vortex control in simulated sail-hull interaction," *Journal of ship research*, Vol. 31, No. 2, 1987, pp. 136–138.

- [7] Gupta, A., "Hydrodynamic modification of the horseshoe vortex at a vertical pier junction with ground," *The Physics of fluids*, Vol. 30, No. 4, 1987, pp. 1213–1215. doi:10.1063/1.866270.
- [8] Philips, D., Cimbala, J., and Treaster, A., "Suppression of the wing-body junction vortex by body surface suction," *Journal of aircraft*, Vol. 29, No. 1, 1992, pp. 118–122. doi:10.2514/3.46134.
- [9] Johnson, M., Ravindra, K., and Andres, R., "Comparative study of the elimination of the wing fuselage junction vortex by boundary layer suction and blowing," *32nd AIAA Aerospace Sciences Meeting and Exhibit, Reno NV, January, 1994*, pp. 10–13. doi:10.2514/6.1994-293.
- [10] Seal, C., and Smith, C., "The control of turbulent end-wall boundary layers using surface suction," *Experiments in Fluids*, Vol. 27, No. 6, 1999, pp. 484–496. doi:10.1007/s003480050373.
- [11] Chen, W.-L., Xin, D.-B., Xu, F., Li, H., Ou, J.-P., and Hu, H., "Suppression of vortex-induced vibration of a circular cylinder using suction-based flow control," *Journal of Fluids and Structures*, Vol. 42, 2013, pp. 25–39. doi:10.1016/j.jfluidstructs.2013.05.009.
- [12] LaFleur, R., and Langston, L., "Drag reduction of a cylinder/endwall junction using the iceformation method," *Journal of fluids engineering*, Vol. 115, No. 1, 1993, pp. 26–32. doi:10.1115/1.2910107.
- [13] Kairouz, K., and Rahai, H., "Turbulent junction flow with an upstream ribbed surface," *International journal of heat and fluid flow*, Vol. 26, No. 5, 2005, pp. 771–779. doi:10.1016/j.ijheatfluidflow.2005.02.002.
- [14] Devenport, W. J., Simpson, R. L., Dewitz, M. B., and Agarwal, N. K., "Effects of a leading-edge fillet on the flow past an appendage-body junction," *AIAA journal*, Vol. 30, No. 9, 1992, pp. 2177–2183. doi:10.2514/3.11201.
- [15] Barberis, D., Molton, P., and Malaterre, T., "Control of 3D turbulent boundary layer separation caused by a wing–body junction," *Experimental thermal and fluid science*, Vol. 16, No. 1-2, 1998, pp. 54–63. doi:10.1016/S0894-1777(97)10012-7.
- [16] Van Oudheusden, B., Steenaert, C., and Boermans, L., "Attachment-line approach for design of a wing-body leading-edge fairing," *Journal of aircraft*, Vol. 41, No. 2, 2004, pp. 238–246. doi:10.2514/1.353.
- [17] Wang, J., Bi, W., and Wei, Q., "Effects of an upstream inclined rod on the circular cylinder–flat plate junction flow," *Experiments in fluids*, Vol. 46, No. 6, 2009, pp. 1093–1104. doi:10.1007/s00348-009-0619-4.
- [18] Huang, R., Hsu, C., and Chen, C., "Effects of an upstream tetrahedron on the circular cylinder–flat plate juncture flow," *Experiments in Fluids*, Vol. 56, No. 7, 2015, p. 146. doi:10.1007/s00348-015-2020-9.
- [19] Théberge, M.-A., and Ekmekeci, A., "Effects of an upstream triangular plate on the wing-body junction flow," *Physics of Fluids*, Vol. 29, No. 9, 2017, p. 097105. doi:10.1063/1.5000733.
- [20] Vassberg, J., Sclafani, A., and DeHaan, M., "A wing-body fairing design for the DLR-F6 model: a DPW-III case study," *23rd AIAA Applied Aerodynamics Conference*, 2005, p. 4730. doi:10.2514/6.2005-4730.

- [21] Peigin, S., and Epstein, B., “Aerodynamic optimization of essentially three-dimensional shapes for wing-body fairing,” *AIAA journal*, Vol. 46, No. 7, 2008, pp. 1814–1825. doi:10.2514/1.35465.
- [22] Song, W., and Lv, P., “Two-level wing-body-fairing optimization of a civil transport aircraft,” *Journal of Aircraft*, Vol. 48, No. 6, 2011, pp. 2114–2121. doi:10.2514/1.c031472.
- [23] Brezillon, J., and Dwight, R., “Applications of a discrete viscous adjoint method for aerodynamic shape optimisation of 3D configurations,” *CEAS Aeronautical Journal*, Vol. 3, No. 1, 2012, pp. 25–34. doi:10.1007/s13272-011-0038-0.
- [24] Mykhaskiv, O., Mohanamuraly, P., Mueller, J.-D., Xu, S., and Timme, S., “CAD-based shape optimisation of the NASA CRM wing-body intersection using differentiated CAD-kernel,” *35th AIAA Applied Aerodynamics Conference*, 2017, p. 4080. doi:10.2514/6.2017-4080.
- [25] Xu, S., Timme, S., Mykhaskiv, O., and Müller, J., “Wing-body junction optimisation with CAD-based parametrisation including a moving intersection,” *Aerospace Science and Technology*, Vol. 68, 2017, pp. 543–551. doi:10.1016/j.ast.2017.06.014.
- [26] Secco, N. R., Jasa, J. P., Kenway, G. K., and Martins, J. R., “Component-based Geometry Manipulation for Aerodynamic Shape Optimization with Overset Meshes,” *AIAA Journal*, Vol. 56, No. 9, 2018, pp. 3667–3679.
- [27] Belligoli, Z., Koers, A. J., Dwight, R. P., and Eitelberg, G., “Using an Anti-Fairing to Reduce Drag at Wing/Body Junctions,” *AIAA Journal*, Vol. 57, No. 4, 2018, pp. 1468–1480. doi:10.2514/1.J057481.
- [28] van Oudheusden, B., Scarano, F., Roosenboom, E., Casimiri, E., and Souverein, L., “Evaluation of integral forces and pressure fields from planar velocimetry data for incompressible and compressible flows,” *Experiments in Fluids*, Vol. 43, No. 2-3, 2007, pp. 153–162. doi:10.1007/s00348-007-0261-y.
- [29] Fleming, J., Simpson, R., Cowling, J., and Devenport, W., “An experimental study of a turbulent wing-body junction and wake flow,” *Experiments in fluids*, Vol. 14, No. 5, 1993, pp. 366–378. doi:10.1007/BF00189496.
- [30] Palacios, F., Colonno, M., Aranake, A., Campos, A., Copeland, S., Economon, T., Lonkar, A., Lukaczyk, T., Taylor, T., and Alonso, J., “Stanford University Unstructured (SU2): An open-source integrated computational environment for multi-physics simulation and design,” *AIAA Paper*, Vol. 287, 2013. doi:10.2514/6.2013-287.
- [31] Economon, T. D., Palacios, F., Copeland, S. R., Lukaczyk, T. W., and Alonso, J. J., “SU2: An open-source suite for multiphysics simulation and design,” *Aiaa Journal*, Vol. 54, No. 3, 2016, pp. 828–846.
- [32] Vitale, S., Gori, G., Pini, M., Guardone, A., Economon, T. D., Palacios, F., Alonso, J. J., and Colonna, P., “Extension of the su2 open source cfd code to the simulation of turbulent flows of fluids modelled with complex thermophysical laws,” *22nd AIAA Computational Fluid Dynamics Conference*, 2015, p. 2760.
- [33] Apsley, D., and Leschziner, M., “Investigation of advanced turbulence models for the flow in a generic wing-body junction,” *Flow, Turbulence and Combustion*, Vol. 67, No. 1, 2001, pp. 25–55. doi:10.1023/A:1013598401276.

- [34] Hickel, S., Adams, N. A., and Domaradzki, J. A., “An adaptive local deconvolution method for implicit LES,” *Journal of Computational Physics*, Vol. 213, No. 1, 2006, pp. 413–436. doi:10.1016/j.jcp.2005.08.017.
- [35] Hickel, S., Egerer, C. P., and Larsson, J., “Subgrid-scale modeling for implicit large eddy simulation of compressible flows and shock-turbulence interaction,” *Physics of Fluids*, Vol. 26, No. 10, 2014, p. 106101. doi:10.1063/1.4898641.
- [36] Meyer, M., Devesa, A., Hickel, S., Hu, X., and Adams, N. A., “A conservative immersed interface method for large-eddy simulation of incompressible flows,” *Journal of Computational Physics*, Vol. 229, No. 18, 2010, pp. 6300–6317. doi:10.1016/j.jcp.2010.04.040.
- [37] Shih, T.-H., *A generalized wall function*, National Aeronautics and Space Administration, Glenn Research Center, 1999.
- [38] Srikumar, S., “LES of a novel wing/body junction: Anti-fairing,” Master’s thesis, TU Delft, 2019. UUID: 86621aa3-90a6-4929-9534-97459ef11f87.
- [39] Ryu, S., Emory, M., Iaccarino, G., Campos, A., and Duraisamy, K., “Large-Eddy Simulation of a Wing–Body Junction Flow,” *AIAA Journal*, Vol. 54, No. 3, 2016, pp. 793–804. doi:10.2514/1.J054212.
- [40] Hoffmann, P., Muck, K., and Bradshaw, P., “The effect of concave surface curvature on turbulent boundary layers,” *Journal of Fluid mechanics*, Vol. 161, 1985, pp. 371–403.
- [41] Muck, K., Hoffmann, P., and Bradshaw, P., “The effect of convex surface curvature on turbulent boundary layers,” *Journal of Fluid Mechanics*, Vol. 161, 1985, pp. 347–369.
- [42] Moser, R. D., and Moin, P., “The effects of curvature in wall-bounded turbulent flows,” *Journal of Fluid Mechanics*, Vol. 175, 1987, pp. 479–510.
- [43] Gillis, J., and Johnston, J., “Turbulent boundary-layer flow and structure on a convex wall and its redevelopment on a flat wall,” *Journal of Fluid Mechanics*, Vol. 135, 1983, pp. 123–153.
- [44] Bandyopadhyay, P. R., and Ahmed, A., “Turbulent boundary layers subjected to multiple curvatures and pressure gradients,” *Journal of Fluid Mechanics*, Vol. 246, 1993, pp. 503–527.
- [45] Menter, F. R., Kuntz, M., and Langtry, R., “Ten years of industrial experience with the SST turbulence model,” *Turbulence, heat and mass transfer*, Vol. 4, No. 1, 2003, pp. 625–632.
- [46] “Dimple Technologies Website,” www.dimple-technologies.com, 2020.
- [47] Bosbach, J., Kühn, M., and Wagner, C., “Large scale particle image velocimetry with helium filled soap bubbles,” *Experiments in fluids*, Vol. 46, No. 3, 2009, pp. 539–547.
- [48] Faleiros, D. E., Tuinstra, M., Sciacchitano, A., and Scarano, F., “Generation and control of helium-filled soap bubbles for PIV,” *Experiments in Fluids*, Vol. 60, No. 3, 2019, p. 40.
- [49] Yeung, K. H., “Characterization of junction flow under the influence of passive flow control devices: An experimental study with large-scale tomographic PTV technique,” Master’s thesis, TU Delft, 2017. UUID: f934cee3-443d-411e-bbde-3c284f6ee4c7.